

Functionalized helical fibre bundles of carbon nanotubes as electrochemical sensors for long-term in vivo monitoring of multiple disease biomarkers

Liyuan Wang^{1,4}, Songlin Xie^{1,4}, Zhiyuan Wang^{2,4}, Fei Liu³, Yifan Yang³, Chengqiang Tang¹, Xiaoying Wu¹, Peng Liu¹, Yongjing Li¹, Hexige Saiyin², Shuang Zheng¹, Xuemei Sun^{1*}, Fan Xu^{3*}, Hongbo Yu^{2*} and Huisheng Peng^{1*}

Mechanical mismatches between implanted electronics and biological tissues can lead to inaccurate readings and long-term tissue damage. Here, we show that functionalized multi-walled carbon nanotubes twisted into helical fibre bundles that mimic the hierarchical structure of muscle can monitor multiple disease biomarkers in vivo. The flexible fibre bundles are injectable, have a low bending stiffness and display ultralow stress under compression. As proof-of-concept evidence of the sensing capabilities of these fibre bundles, we show that the fibre bundles enable the spatially resolved and real-time monitoring of H₂O₂ when implanted in tumours in mice, and that they can be integrated with a wireless transmission system on an adhesive skin patch to monitor calcium ions and glucose in the venous blood of cats for 28 d. The versatility of the helical fibre bundles as chemically functionalized electrochemical sensors makes them suitable for multiple sensing applications in biomedicine and healthcare.

Implantable electronic devices, such as sensors and probes, have enabled the precise measurement of biological activities^{1–4} and treatments to be delivered to a specific location^{5–8}. However, most sensors that work stably in vitro cannot adapt to the physically dynamic and biochemically complicated environment in vivo⁹. Biological tissues are soft, curvilinear and transient, whereas current flexible sensors made from monolithic membrane substrates with large sizes, such as polyimide (PI)¹⁰, show high bending stiffnesses of more than 10² nN m² that further increase after coating the substrate with conductive and sensing materials. The mechanical mismatch and geometrical structure of these sensors are an obstacle for adaptive conformation to, and synchronized motions with dynamic tissues such as muscle (which has a bending stiffness of less than 10^{–3} nN m²)¹¹. This issue leads to an unstable device–tissue interface, compromises the function and accuracy of the device and damages the tissues over time¹².

Some efforts have been made to overcome the mechanical mismatch by designing mesh geometries and reducing the device dimensions to the cellular level, therefore generating a stable electrode–neuron interface to record electrophysiological signals in the nervous system^{13,14}. For a multiscale mechanical match, mimicking the structure of native tissues may be another promising strategy, considering that a large number of biological tissues (such as muscle, blood vessels and skin) are heterogeneous. Specifically, mechanical properties in many soft tissues such as muscles are achieved through a hierarchical structure¹⁵, in which nanoscale fibrils are assembled into microfibrils, which are in turn assembled into larger fibres (Fig. 1a). Such a hierarchical and helical assembly increases flexibility (lower elastic modulus) because it accommodates reversible deformations and movements among the nanofibrils¹⁶. For

example, a single collagen nanofibril has an elastic modulus of 2.4 GPa (ref. 17), whereas a collagen fibre with a hierarchical structure has a much lower elastic modulus (<25 kPa)¹⁸. Moreover, the device must be biocompatible with cells to integrate with tissues¹⁹. The biomimetic materials with matched microstructures of tissues have been found to recruit nearby extracellular matrix fibres and to promote cell adherence, spreading and proliferation^{20,21}. Finally, independently modified nanofibres were twisted into one assembly, and could therefore serve as simultaneous multiplex sensors. Thus, the bioinspired devices are expected to match the mechanical properties of both tissues and cells to achieve robust and stable biointerfaces for long-term and real-time monitoring of multiple chemicals in body.

Here we show a flexible fibre-based implantable electrochemical sensor that mimics the hierarchical and helical assembly of native soft tissues. The sensor, which was generated by twisting carbon nanotubes (CNTs) into hierarchical and helical bundles of fibres, resembles muscle filaments and matches the bending stiffness of tissues and cells and therefore, provides a flexible, strong and stable fibre–tissue interface. The implantable fibre showed good biocompatibility and was further modified to adapt to applications in vivo. By incorporating different sensing components, various single-ply sensing fibres (SSFs) were fabricated for specific chemical detection. Twisting multiple SSFs together resulted in multi-ply sensing fibres (MSFs). By applying different functional SSFs in an MSF, we can realize real-time simultaneous detection of multiple biomarkers in vivo. By distributing SSF terminals with exquisite spatial resolution, MSFs could provide a μm -scale spatial gradient map of a single biomarker in tissues. Furthermore, the one-dimensional configuration of the sensing fibres enables a syringe-assisted implantation method, which is much less invasive than the surgery that is required

¹State Key Laboratory of Molecular Engineering of Polymers, Department of Macromolecular Science and Laboratory of Advanced Materials, Fudan University, Shanghai, China. ²Vision Research Laboratory, School of Life Sciences, State Key Laboratory of Medical Neurobiology, Collaborative Innovation Centre for Brain Science, Fudan University, Shanghai, China. ³Department of Aeronautics and Astronautics, Fudan University, Shanghai, China. ⁴These authors contributed equally: Liyuan Wang, Songlin Xie, Zhiyuan Wang. *e-mail: sunxm@fudan.edu.cn; fanxu@fudan.edu.cn; hongboyu@fudan.edu.cn; penghs@fudan.edu.cn

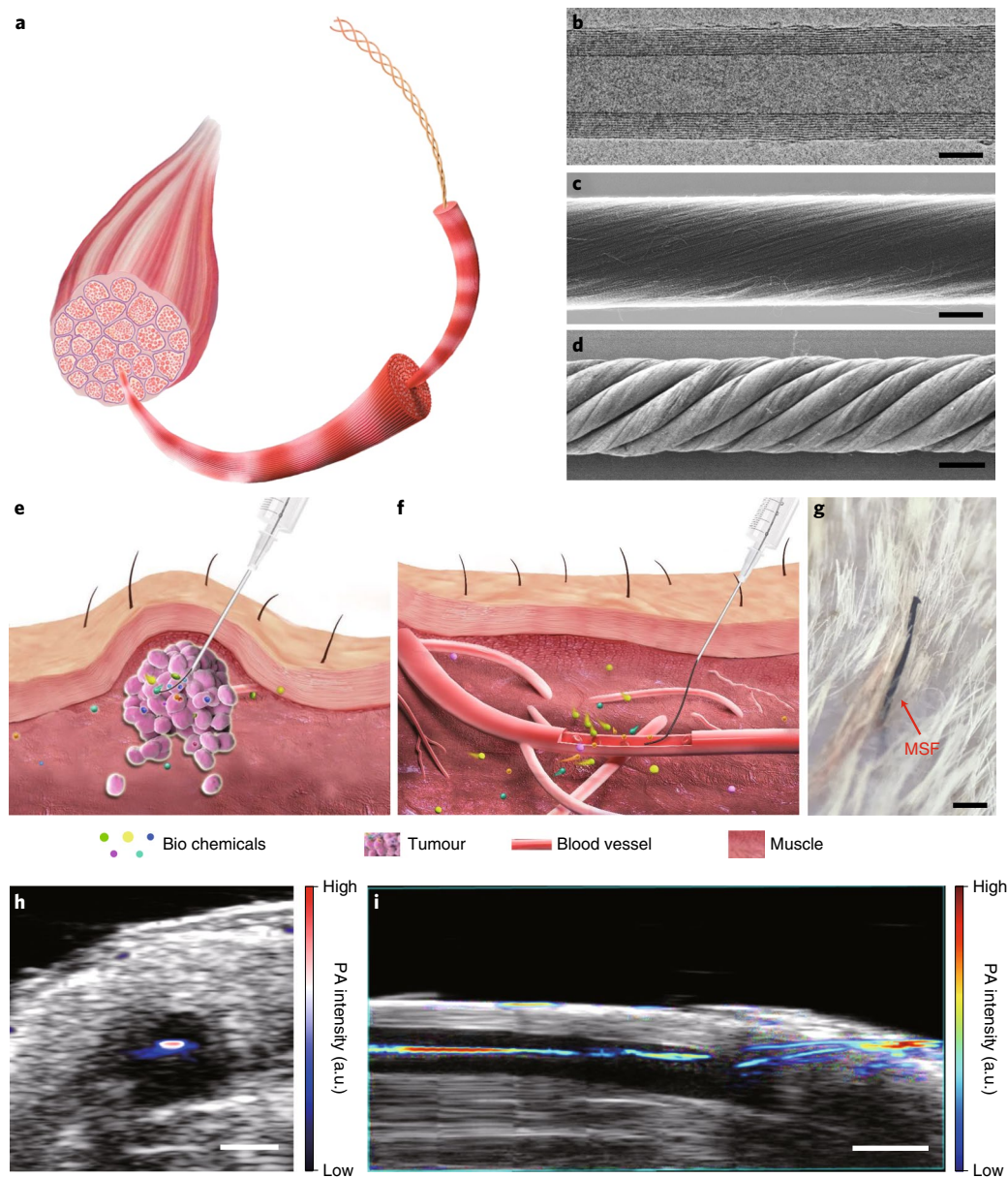


Fig. 1 | Hierarchical helical structure and the implantation of CNT fibre. **a**, Schematic of the hierarchical structure of muscle. **b**, Representative transmission electron microscope image of a multi-walled CNT; three technical repeats were performed. Scale bar, 3 nm. **c,d**, Representative SEM images of a primary CNT fibre (**c**) and a hierarchically helical CNT fibre assembled from primary CNT fibres (**d**); three technical repeats were performed. Scale bars, 6 μm (**c**) and 20 μm (**d**). **e,f**, Schematics showing the injection of the fibre into a target tumour (**e**) and blood vessel (**f**). **g**, Photograph of the skin surface of a cat after injection with a MSF. Scale bar, 500 μm . **h,i**, PA images of the vein of a cat after MSF injection in top (**h**) and side (**i**) views; six technical repeats were performed. Scale bars, 700 μm (**h**) and 2 mm (**i**).

for film-shaped devices²². By using this method, we show that the fibre could be delivered to any target region regardless of surface topography and detection depth, offering a potential approach for the comprehensive monitoring of key metabolites in the body.

A structurally and mechanically matching CNT fibre

Multi-walled CNTs with diameters of 8–15 nm were synthesized using chemical vapour deposition, and the hierarchical CNT fibres were fabricated by twisting the CNTs into helical bundles (Fig. 1b–d; details are provided in Supplementary Methods 1). The fibres, with controlled diameters ranging from one to hundreds of μm , are mechanically compliant, lightweight and flexible (Supplementary Fig. 1).

To deliver flexible electronic devices to target tissues with minimal or non-invasive effects other than surgical insertion, it is highly desirable to miniaturize the devices and develop proper implantation techniques. Two methods of microfluidic actuation²³ and syringe injection²⁴ with the assistance of the fluid have been introduced to precisely deliver materials and devices to target tissues, including vulnerable tissues such as the brain. The thin CNT fibre with a one-dimensional configuration may better fit (or even perfectly fit) the syringe needle such that one end of the fibre can be precisely injected into the target tissues while the other end of the fibre remains outside the tissue for external connection after removal of the syringe. The fibres could therefore be properly injected into target tissues such as tumours (Fig. 1e) and blood vessels (Fig. 1f).

We evaluated the injectability of the CNT fibres in vivo by injecting a single fibre in a syringe with 300 μl saline at a velocity of 1.0 mm s^{-1} into the femoral vein of a cat. The slow insertion speed rendered a shallow force and prevented inadvertent tissue damage. After the flexible fibre was injected into the cat by intravenous injection, it appeared almost like a hair on the skin (Fig. 1g). The intense infrared absorption of CNTs enabled us to use photoacoustic (PA) imaging to determine the position and structural changes in vivo after implantation (Supplementary Fig. 2a). Three-dimensional reconstruction images showed that the CNT fibre penetrated the skin and was surrounded by neighbouring tissues (Supplementary Fig. 2b), which kept the fibre stable in the centre of the blood vessel under blood flush (Fig. 1h,i).

Compared with the surgical insertion of soft polymer films, such as polydimethylsiloxane (PDMS)-based sensors, which require a large incision and longer healing time, the wound around the injected CNT fibre on the skin surface was only tens of μm larger than the radius of the fibre after injection and usually recovered within 10 min (Supplementary Fig. 3). No sign of infection or abnormality was detected during 4 d after the injection (Supplementary Fig. 4). The fluctuation of blood flow after implanting two cats with CNT fibre for 5 d was within the fluctuation range of normal cats without CNT fibre (Supplementary Fig. 5). After the removal of the CNT fibre, the wound healed rapidly within 2 d (Supplementary Fig. 6).

A mechanical match between tissue and device is essential for safe and accurate readings. Lots of tissues, such as muscle, skin and blood vessels, are usually heterogeneous. Mechanical properties therefore differ between macroscopic and cellular scales. For example, the elastic moduli of muscle tissues are ~ 480 MPa at the macroscopic scale using the tensile method and ~ 7 kPa using the indentation method, possibly reflecting the cellular properties²⁵. The elastic moduli of cells were also reported to be 0.1–100 kPa (ref. 26). For the implants that work typically with cells, concerning the interface, it is important that the implants match the bending stiffness at the cellular scale. To this end, we used the nanoindentation method to test the moduli of our fibre and other common fibres to compare the bending stiffnesses at the cellular scale (Supplementary Table 1). The bending stiffness of the CNT fibre was much lower than those of similar sizes of silicon, gold and carbon fibre (CF; Fig. 2a), and it could be adapted to the range of bending stiffnesses for most tissues, such as muscles and blood vessels, by varying its diameter. Bending stiffnesses based on the tensile method were also compared for the CNT fibre using state-of-art implantable devices and tissues, which are described in Supplementary Table 2, and the bending stiffness of the CNT fibre also matched those of most tissues. The bending stiffness of the CNT fibre can be explained by its small size and hierarchical structure. This flexibility allows the fibres to conform to different tissues from micro to macro scale and withstand the dynamic environments inside the body.

During movements, any pressure applied through the skin and cardiac/respiratory pulsations will be transferred to tissues and implanted devices as well. This means that, to achieve a stable fibre–tissue interface, the fibre should generate only a small amount of internal stress under deformation. To determine the extent of the lesion that the CNT fibre inflicts onto the surrounding tissues, we examined the internal stress generated in the fibre under compression. The CNT fibres with a length of 4 mm were compressed from one end using a Nano-tensile machine and showed stresses of around 104 kPa, which is orders of magnitude smaller than those of conventional implanted materials (Fig. 2b, Supplementary Fig. 7). Such a low force avoided the potential for injury to surrounding tissues and maintained a stable fibre–tissue interface. To elucidate the underlying mechanism of the reduced internal stress, we used the finite element method to simulate the stress field in fibres consisting of different building blocks under compression (Supplementary

Fig. 8). The fibre assembled from nanotubes with a certain void ratio showed much lower stress and a more uniform stress distribution than the fibre without nanostructure under the same compression (Fig. 2c, Supplementary Fig. 9). We found that the stress of the fibre and its distribution were also related to the aspect ratio of length to diameter in nanotubes. A higher aspect ratio produced lower stress (Supplementary Fig. 10). Overall, a fibre that is hierarchically assembled from one-dimensional nanomaterials is an effective strategy to generate high flexibility to adapt to the soft tissues.

When the CNT fibre was inserted into fresh cardiac muscle tissue of a pig, the fibre and tissue formed and maintained a close contact even under repeated elongation and twisting processes, observed from the PA three-dimensional reconstruction image (Fig. 2d). The CNT fibre was also injected into a fresh pig brain (Fig. 2e, i). When applying a compression force on the cortex (arrow position in Fig. 2e, ii), we found that the exterior length of the CNT fibre remained unchanged, indicating that no obvious sliding had occurred. Furthermore, when we extracted the CNT fibre and compared the contour lines of the cortex and CNT fibre, deformation was seen only at the site at which force was applied (Fig. 2e, iii–v, around the arrow). Overall, a stable device–tissue interface was observed during both twisting and bending. The distribution of the interaction force at the device–tissue interface was further simulated using the finite element method. A medium was chosen with the same mechanical properties as muscles and the implantable materials were then inserted into the medium. Different motions of the tissue implanted with materials were simulated by changing the type of load on the medium. When the medium was twisting, as shown in the cardiac muscle in Fig. 2d (i), the CNT fibre followed and only generated an interfacial stress of 10–15 MPa, which is lower than the interfacial stress generated by other implantable materials, including CF (300–1,100 MPa) and PI film (125–570 MPa; Fig. 2f, Supplementary Fig. 11). As for bending, the CNT fibre showed uniform interfacial stress of 20–30 MPa. By contrast, the monolithic fibre, such as CF, and polymer film, such as PI, caused severe stress concentration near the edge that could induce trauma to the neighbouring tissues (Fig. 2g, Supplementary Fig. 12).

The toxicity²⁷ and immune response²⁸ of the devices were further evaluated to ensure the safe application in vivo. At first, cell experiments showed a similar proliferation rate of L929 cells between CNTs and the control group (Fig. 2h,i, Supplementary Figs. 13 and 14). The long-term safety in vivo was then verified by the histological analysis of organs, including liver, lungs, kidney, spleen and cardiac muscles, after implanting CNT fibres in blood vessels for 21 d; no CNT residues could be identified (Supplementary Fig. 15). Inflammatory cells were stained for CD11b expression (a neutrophil marker) to monitor the possible immune response. No significant differences were found in the fluorescence signals between the surrounding muscle tissue after 21 d of CNT fibre implantation and the control group without implants (Fig. 2j,k). Furthermore, haematoxylin and eosin (H&E) staining showed that the tissue morphology around the CNT fibre was similar to the control group after 21 d, indicating good integration between the fibre and the tissue (Fig. 2l,m). Masson's trichrome staining also showed that the CNT fibre could be normally encapsulated by myocytes and no obvious scar formation was found (Supplementary Fig. 16a). By contrast, a gold wire with a similar size showed a higher intensity of immune response after 5 d implantation (Supplementary Fig. 17) and was encapsulated by collagen fibres after 21 d, indicating potential scar formation²⁹ (Supplementary Fig. 16b). These combined results suggested that the CNT fibre is biocompatible with tissues and does not elicit unusual and chronic immune responses after implantation.

Preparation of various sensing fibres

We used the CNT fibres to develop various sensing systems for in vivo applications. In contrast to the bare electrical signal for

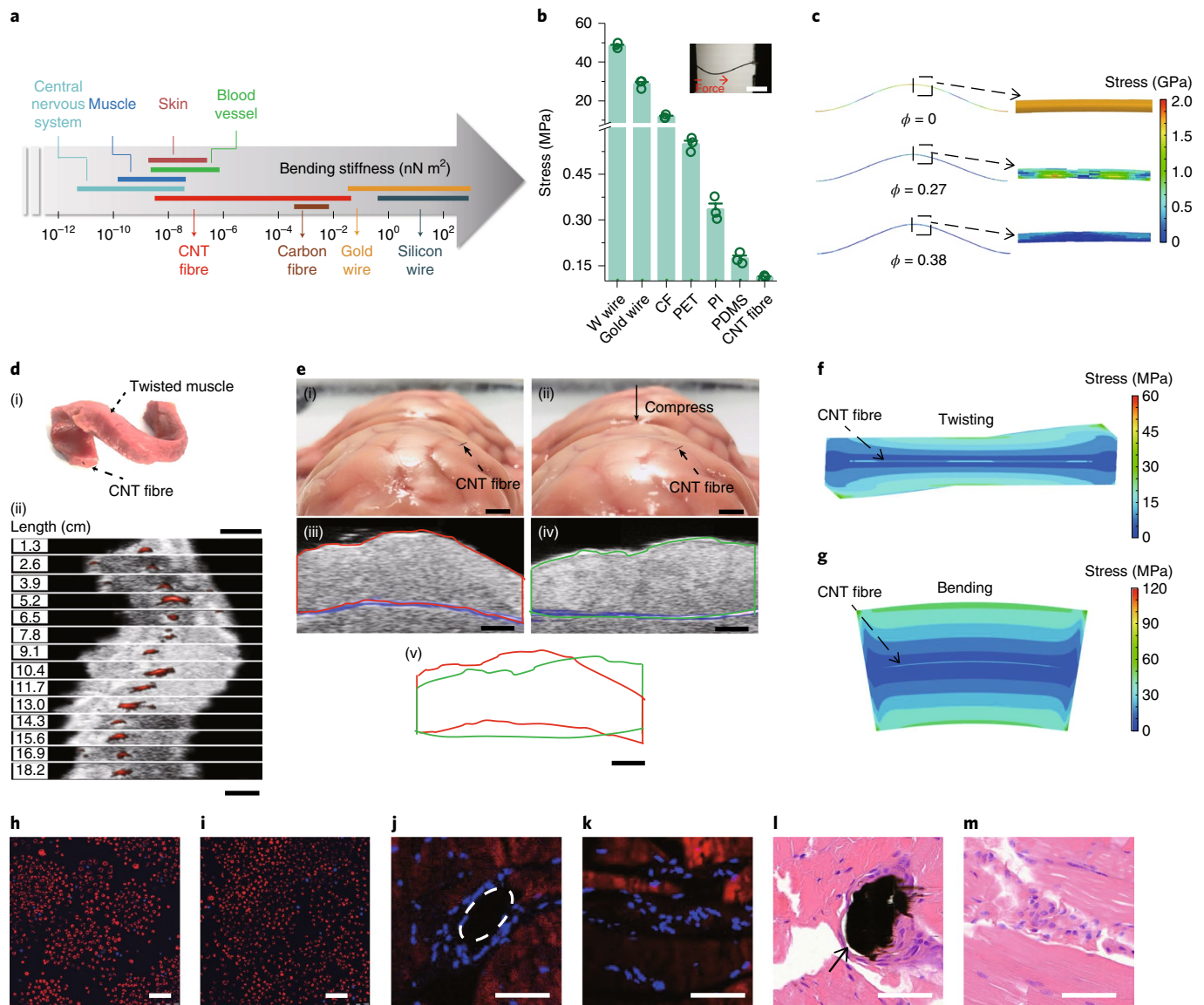


Fig. 2 | Mechanical match, biocompatibility and biointegration of the implanted CNT fibre. **a**, Comparison of the CNT fibre with other implantable materials, such as CF, gold wire and silicon wire. The bending stiffnesses of CNT fibres match a range of soft tissues. The elastic moduli were measured using the nanoindentation method. The lines indicate the measured result and the bars represent the calculated range of bending stiffnesses of each material. **b**, The internal stress of the CNT fibre under compression compared with other implanted materials, including tungsten (W) wire, gold wire and CF with a diameter of $\sim 50\ \mu\text{m}$, polyethylene terephthalate (PET) film, PI film and PDMS film with a section size of $50\ \mu\text{m} \times 5\ \text{mm}$; three technical repeats were performed. Data are mean \pm s.d. Inset: the typical setup for the test; the red dashed arrow indicates the direction of applied force. Scale bar, 1 mm. **c**, The stress distribution simulation of the CNT fibre with different void ratios of the cross-section under the same compression, for which the void ratio of the cross-section (ϕ) is defined as the void area (S_v) over the entire cross-sectional area (S): $\phi = S_v/S$. **d**, Photograph (i) and the corresponding PA image (ii) of a piece of twisted fresh cardiac muscle, which was injected with a CNT fibre, from a pig. The red regions in ii indicate the location of CNT fibres. The numbers on the left represent physical length. Scale bars, 2 cm (i) and 3 mm (ii). **e**, Optical images (i and ii) and the corresponding PA images (iii and iv) of an unprocessed fresh brain, which was implanted with a CNT fibre, from a pig before (i and iii) and after (i and iv) compression. Contour lines (v) extracted from PA images in iii and iv. Scale bars, 1 cm (i and ii), 2 mm (iii–v). **f, g**, The stress simulation of the CNT fibre in a tissue-like medium with similar mechanical properties of muscle under twisting (**f**) and bending (**g**), showing a very low level of stress with a uniform distribution around the fibre. **h, i**, Merged confocal images of L929 cells cultured 5 d on CNTs (**h**) and glass as a control (**i**) showing no significant differences between the substrates. Two technical repeats were performed. Living cells are indicated in red (Cellbrite Red), dead cells are indicated in blue (Nuclear Blue DCS1). Scale bars, 100 μm . **j, k**, A CD11b-labelled section of muscle tissues, which were implanted with CNT fibre after implantation of 21 d (**j**) and non-implanted control samples (**k**); five technical repeats were performed. The nucleus is shown in blue (DAPI) and CD11b is shown in red. The positively labelled cells are double stained by both DAPI and anti-CD11b antibodies. The white dotted line indicates the position of CNT fibres. Scale bars, 50 μm . **l, m**, Representative H&E sections of muscle tissues implanted with CNT fibre after implantation of 21 d (**l**) and non-implanted control samples (**m**); five technical repeats were performed. The black arrow indicates the position of the CNT fibre. Scale bars, 50 μm .

neural recording, chemical sensing requires the modification of fibre electrodes with active materials. Owing to their high surface roughness, large specific surface area and remarkable electrochemical properties, CNT fibres can be easily modified with different func-

tional groups and/or incorporated with a second component, such as polymers, metal, metal oxide and biomolecules. Modifications can be made using physical evaporation techniques, electrochemical deposition, in situ polymerization and/or dip-coating³⁰. For

example, Pt nanoparticles could be easily electrodeposited into CNT fibres to form uniform and stable hybrid materials, whereas the Pt nanoparticles were less uniform and easy to peel off CF and gold wire under the same conditions (Supplementary Figs. 18 and 19). Many complicated sensing systems can therefore be obtained by designing coaxial laminated structures comprising an electrode, a signal-transforming layer, a responsive layer and an insulating layer. Furthermore, by coating or modifying the fibres with a range of functional layers, it is possible to obtain multiplex sensors that can detect various physiological signals ranging from neurotransmitters, to nutritional status to metabolites and, therefore, a 'SSF library' can be established.

As a proof of concept, we developed four basic electrochemical sensors that can detect ions and prostate-specific antigens (PSAs) through impedance change, as well as hydrogen peroxide (H_2O_2) and glucose through redox reactions. First, the reference electrode was prepared by electrodepositing Ag/AgCl onto CNT fibres, followed by coating a polymer layer for biocompatibility (Supplementary Figs. 20 and 21). The H_2O_2 SSF has the simplest structure with Pt nanoparticles electrochemically deposited into the CNT fibre (Fig. 3a, i and ii). As the Pt nanoparticles catalysed the dissociation of H_2O_2 , electron transfer occurred along the fibre. Current response of the H_2O_2 SSF measured in 0–50 μM H_2O_2 aqueous solution showed a sensitivity of approximately 0.84 $\mu\text{A} \mu\text{M}^{-1}$ and a linear range from 0 to 1.0 mM (Fig. 3a, iii and iv). The performance of the CNT fibres was also highly reproducible (Supplementary Fig. 22). The PSA SSFs with more complex structures were prepared by dip-coating chitosan- $\text{Pb}_2[\text{Fe}(\text{CN})_6]$ -poly(diallyldimethylammonium chloride)-graphene oxide aqueous solution onto the CNT fibre and coating the outside with PSA-selective membrane to detect the antigen (Fig. 3b, i and ii). The PSA SSF showed a low detection limit of $10^{-7} \text{ ng ml}^{-1}$ and a sensitivity of approximately 0.17 $\mu\text{A ng}^{-1} \text{ ml}$; Fig. 3b, iii and iv). The PSA SSF can be used to detect PSA levels in blood (normal physiological levels, $<0.5 \text{ ng ml}^{-1}$; pathological state at high risk of death, $>2.0 \text{ ng ml}^{-1}$)³¹. The Ca^{2+} SSFs had a similar structure to the PSA SSF. In this case, a CNT fibre was dip-coated with a poly(3,4-ethylenedioxythiophene)-poly(styrenesulfonate) (PEDOT:PSS) solution (Supplementary Fig. 23), followed by a Ca^{2+} -selective membrane cocktail to form a uniform and Ca^{2+} -specific adsorptive layer (Fig. 3c, i and ii). The subtle potential field change along with Ca^{2+} flow could be collected by the electrode. The open-circuit potential of the Ca^{2+} SSF was measured in 0.5–2.5 mM Ca^{2+} electrolyte with a sensitivity of $\sim 4.0 \text{ mV mM}^{-1}$ and proper selectivity with negligible interference from the other non-target materials (Fig. 3c, iii and iv; Supplementary Fig. 24). The sensors for other ions, such as Na^+ , K^+ and pH, could also be fabricated using a similar method. SSFs with more complicated structures, such as glucose SSFs, can be generated using layer-by-layer coating processes. Taking enzyme-based glucose SSF (Fig. 3d, i and ii) as an example, a signal-transforming layer composed of polyaniline (PANI) and Pt nanoparticles was first electrochemically deposited into the core CNT fibre electrode. This layer converted concentrations of H_2O_2 intermediates into electrical current signals. Subsequently, the fibre was dip-coated with a glucose-responsive layer made of glucose oxidase immobilized on a linear polysaccharide chitosan. Finally, Nafion and glutaraldehyde was used to produce micropores to improve the selectivity and stability of the sensor (Supplementary Fig. 25). The glucose SSF had a working range of 2.5–7.0 mM, matched with the humoral glucose level (Supplementary Fig. 26). The glucose sensor had a sensitivity of $\sim 5.6 \text{ nA} \mu\text{M}^{-1}$ and a low detection limit of 50 μM (Fig. 3d, iii and iv), which is comparable to the state-of-art planar glucose sensor³² and far exceeded a commercial glucometer. Importantly, the measurements were highly reproducible with different fibres, although the fabrication process was complicated. Non-enzyme glucose SSFs can also be prepared on the basis of inorganic materials, such as ZnO nanoparticles. Here

we prepared ZnO-based glucose SSFs and used them for long-term glucose monitoring.

As extracellular fluids contain multiple biological labels and can be unevenly distributed in various tissues and undergo transient change³³, we further fabricated MSFs with different geometrical structures that were suitable for spatial analysis and real-time multiplex monitoring. For spatial analysis, several primary SSFs were twisted together with a common reference fibre electrode to obtain an MSF with a fibre terminal that was regularly spaced along the axial direction. Terminal configuration of the MSF could be mediated by the angle between the primary SSFs and the twisting motor, and the patch distance between two neighbouring SSFs could be controlled by the rotation angle and diameter of the individual SSFs. When the same type of SSF was used and axially distributed in the MSF, the distribution of target analytes could be obtained with a spatial resolution that was tuneable from μm (comparable to the diameter of the fibre) to mm (Fig. 3e).

Body fluid is composed of multiple chemicals and the ability to monitor several of these chemicals simultaneously in real time is desirable for understanding how they change and interact with each other over time. To demonstrate multiplex monitoring, we selected SSFs that detect several representatives of nutrition, electrolyte and metabolites from the SSF library. After twisting different types of SSF together with a reference fibre electrode, we obtained an MSF with radially distributed ends (Fig. 3f). Each SSF at the terminal end of the MSF detected different target analytes. For example, glucose, Ca^{2+} , Na^+ , K^+ and pH SSFs were prepared and twisted with an Ag/AgCl reference electrode. To avoid cross-talk or signal interference, each SSF in MSF was encapsulated by a PDMS layer with a thickness of around 6 μm (Supplementary Fig. 27). All of the SSFs were tested separately and integrally in the MSF. Owing to the effective encapsulation, each SSF in the MSF could work effectively in the mixed solution of multiplex analytes (Supplementary Fig. 28). Furthermore, five H_2O_2 SSFs were prepared and tested with varying distances among them, and the impedance of individual SSFs remained unchanged with increasing distance (Supplementary Fig. 29). These results suggest that there is no obvious cross-talk among sensors and verified the feasibility and robustness of MSF designs.

The structural, mechanical and electrical stability of MSFs

For long-term effective *in vivo* application, structural, mechanical and electrical stability are required under humoral conditions. The as-fabricated MSF was kept in a polyacrylamide hydrogel that mimics the physiological state at 37°C, the twisted structure was well reserved after 7 d (Fig. 4a,b). An MSF was then injected into the femoral vein of a cat. Over 5 d, fibre morphology extracted from PA images showed no distinct changes in length (Fig. 4c). When removed, the mechanical strength was found to be well maintained (Fig. 4d, Supplementary Fig. 30a). Most fibres demonstrated strengths of $\sim 350 \text{ MPa}$ at $\sim 7\%$ strain. Together, these results show that the hierarchical structure of the MSF and its mechanical properties are stable and could tolerate the continuous fluid flow *in vivo*, making them suitable for long-term applications.

For electrochemical stability and robustness, both the humoral conditions and tissue dynamics must be taken into consideration. The impedance over a range of frequencies is a typical indicator for electrochemical systems because it reflects not only the internal structural changes of active materials and electrodes in devices but also the interfaces between the devices and tissues. The interface could be influenced by the external adsorption of macromolecules such as proteins and the attachment of cells³⁴. The impedance can therefore be used to evaluate the electrochemical stability of sensors, and a typical Nyquist plot of a SSF is shown in Supplementary Fig. 31. The impedance magnitude of each SSF remained almost unchanged after bending and twisting for 100 cycles, with an impedance fluctuation of $\pm 0.35\%$ (Fig. 4e,f, Supplementary Fig. 30b,c).

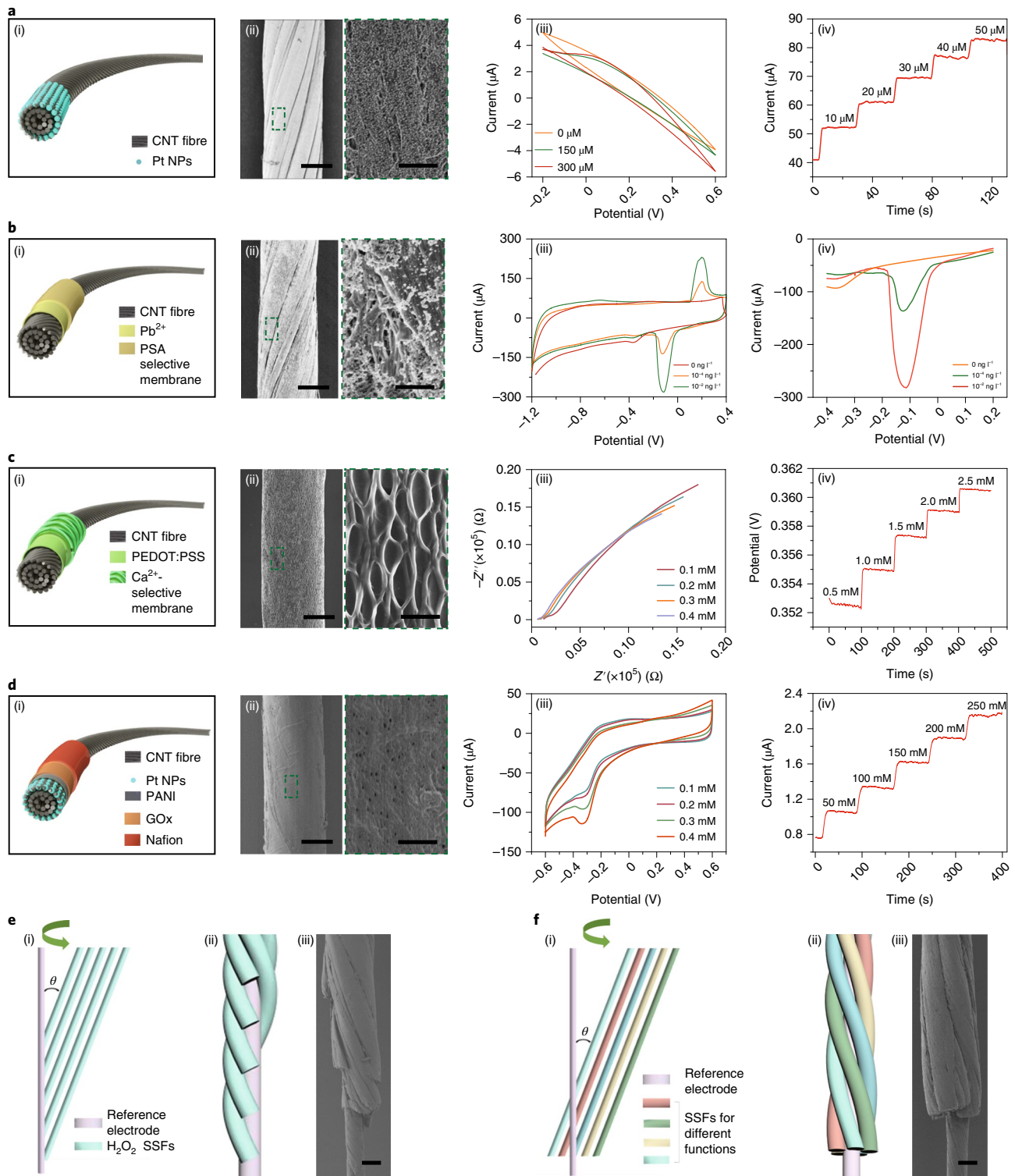


Fig. 3 | The structure and performance of the SSF library and the fabrication of MSFs. a–d, The structure and performance of H₂O₂ (**a**), PSA (**b**), Ca²⁺ (**c**) and glucose (**d**) SSFs. Schematic of the layered composition of SSFs (i). Representative SEM images of SSFs (ii, left) and magnified images of SSF surface morphology (ii, right) within the region indicated by green rectangles on the left; three technical repeats were performed. Scale bars, 25 μm (ii, left) and 1 μm (ii, right). Cyclic voltammetry (**a,b,d**, iii) and electrochemical impedance spectra change (**c**, iii) with increasing concentrations; three technical repeats were performed. The chronoamperometric (**a,b,d**, iv) and open-circuit potential responses (**c**, iv) at different concentrations of analyte, indicating the sensitivity of SSFs; three technical repeats were performed. NPs, nanoparticles. Impedance is a two-dimensional quantity comprising resistance (real component vector, Z') and reactance (imaginary component vector, Z''). **e**, Schematic of the preparation process (i), schematic of the structure (ii) and a representative SEM image (iii) of an MSF with axial terminals and five evenly spaced SSFs for spatial analysis; three technical repeats were performed. Scale bar, 50 μm. **f**, Schematic of the preparation process (i), schematic of the structure (ii) and a representative SEM image (iii) of an MSF with radial terminals for multiplex monitoring, such as glucose, Ca²⁺, Na⁺, K⁺ and pH; three technical repeats were performed. Scale bar, 50 μm. The green arrows in **e** and **f** indicate the twisting direction of the motor during preparation.

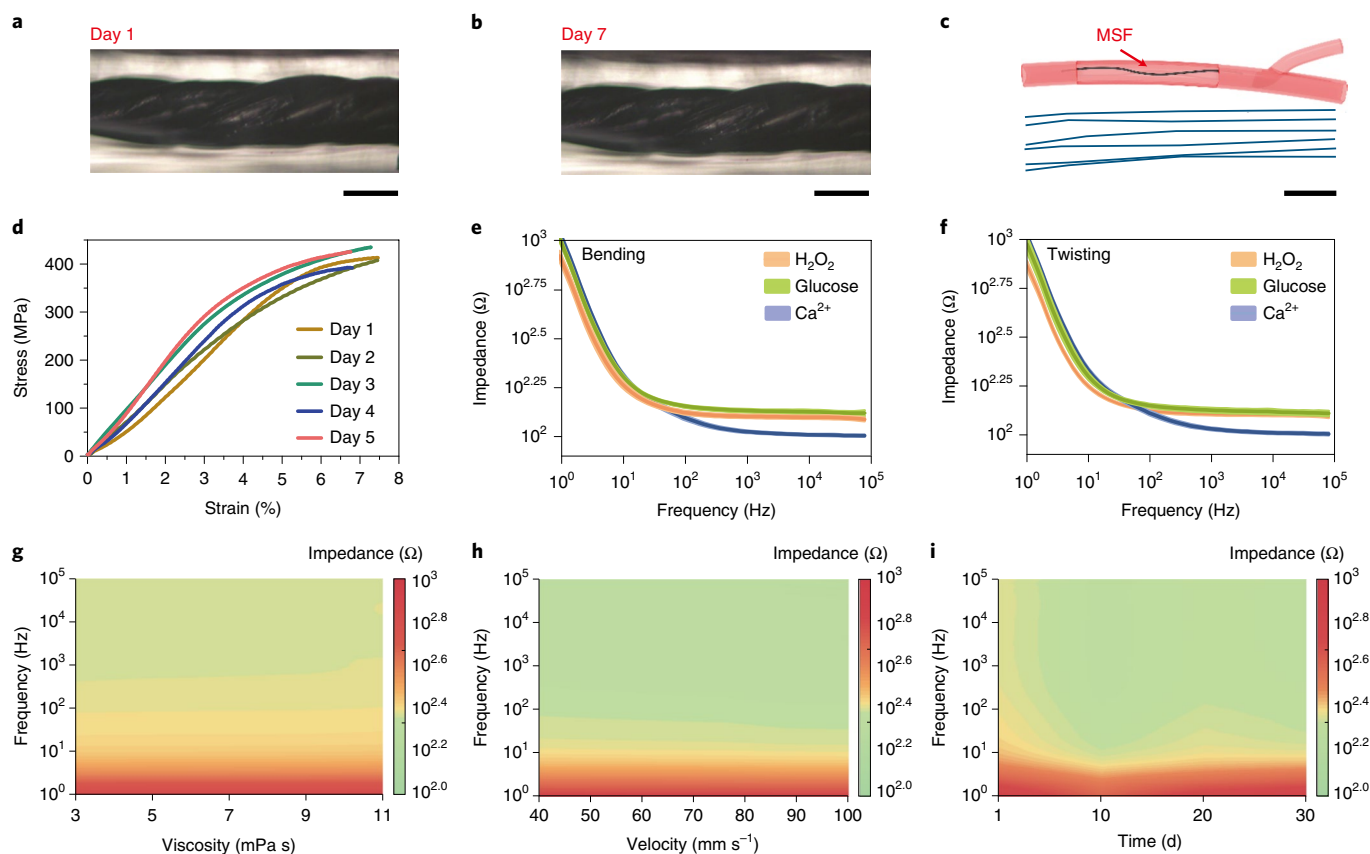


Fig. 4 | The structure and stability of the MSF. **a,b**, Optical images of an MSF in a polyacrylamide hydrogel on day 1 (**a**) and 7 (**b**) with a constant temperature of 37 °C. No untwisting was seen; two technical repeats were performed. Scale bars, 120 μm. **c**, Schematic of a fibre flowing in the femoral vein of a cat (top) and the extracted PA signals of the MSF in the femoral vein of the cat (blue lines, bottom) for 0–5 d in vivo, showing no change in fibre length. Scale bar, 500 μm. **d**, Representative stress–strain curves of the fibres after injection into a vein of a cat for 1–5 d, showing no obvious changes in tensile strength; three technical repeats were performed. **e,f**, Representative impedance curve of each SSF in an MSF under increasing frequencies of bending (**e**) and twisting (**f**) for 100 cycles, showing no obvious change; three technical repeats were performed. **g,h**, The impedance magnitude changes of an SSF in an MSF, displaying small variations in environments with different viscosities (**g**) and velocities (**h**) (versus the Ag/AgCl electrode). **i**, The impedance magnitude of an SSF in an MSF remains stable in a tube with a flow of PVA/PBS solution for 30 d.

To demonstrate the robustness of our device against the dynamic and versatile microenvironment, we utilized a viscosity-adjustable poly(vinyl alcohol) (PVA)/phosphate-buffered saline (PBS) solution to simulate different tissue conditions while maintaining the viscoelasticity. The SSFs in an MSF displayed non-significant variations in impedance magnitude at viscosities ranging from 3 mPa s to 11 mPa s and velocities ranging from 40 mm s⁻¹ to 100 mm s⁻¹ (Fig. 4g,h). During in vitro long-term tests, SSFs were placed in tubes with similar diameters to blood vessels and flushed by circulating PVA/PBS with similar velocity to the blood. The impedance magnitudes of individual SSFs in the MSF remained stable for over 30 d (Fig. 4i). The residue solution was also collected and measured using an ultraviolet–visible spectrophotometer. No characteristic absorption peaks of CNTs were observed, verifying that rare CNTs had been dissociated from the fibre (Supplementary Fig. 32). These results show that the MSF is electrochemically stable over a broad range of fluid conditions and possible human tissue dynamics and, therefore, meets the challenging requirements for random-target implantation and long-term monitoring³⁴.

MSFs detect the spatial gradient of H₂O₂ in a mouse tumour

Gradient hypoxia is associated with rapid cell growth and distorted vasculature in tumours; however, the spatial distribution of key chemicals in tumours is poorly understood^{35,36}. Using our MSF,

which contained evenly spaced terminal fibres, spatial analysis of chemicals in the tumour microenvironment was possible. To demonstrate this, we twisted five H₂O₂ SSFs with one Ag/AgCl reference electrode to form an MSF with axially distributed ends. An optical image showed that the ends of the SSFs lay uniformly along the axis (Supplementary Fig. 33). The patch distance was adjustable from dozens of μm to a few mm by altering the rotation angle and the initial length of the SSFs. The axial MSF was first injected into agarose gel, and the H₂O₂ was dropped onto the gel from the upper surface (Fig. 5a). Each of the five fibres detected the concentration of H₂O₂ at their own sites, and the H₂O₂ distribution map was obtained over time. As expected from the diffusion model, electrode 1 had a maximum current range (20–240 μA), which corresponded to the H₂O₂ concentration range of 0 mM to 2.75 mM. Similarly, electrodes 2–5 showed current changes of 96.0 μA, 68.8 μA, 32.0 μA and 29.6 μA, which corresponded to H₂O₂ concentration changes of 950 μM, 610 μM, 150 μM and 120 μM, respectively (Fig. 5b). Compared with existing biodetection technologies such as fluorescence³⁷ and PA imaging³⁸, the design of our MSF offers a convenient in situ method to detect analytes in real time with high resolution and rapid feedback.

Next, we injected a H₂O₂ MSF into a solid tumour in a nude mouse using a syringe filled with saline (Fig. 5c). PA signals showed that the longest fibre reached the centre of the tumour (Fig. 5d), whereas the other electrodes laid along the axial direction. We first

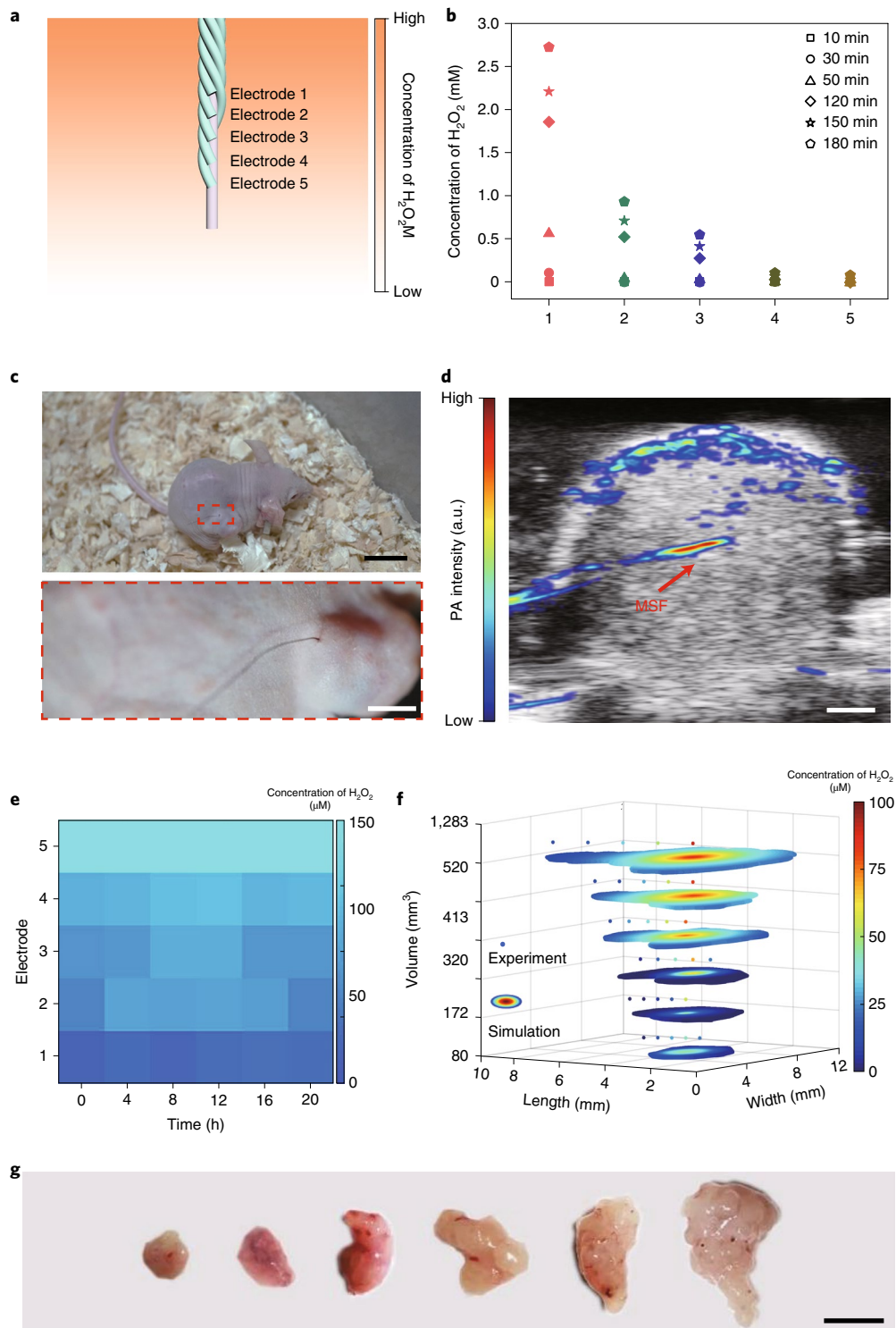


Fig. 5 | The use of MSFs for spatially resolved analysis. **a**, Schematic of a MSF that was used for spatial analysis in a concentration-gradient environment. The colour from light to dark indicates an increase in the concentration of H_2O_2 . **b**, The distance–concentration plot of the H_2O_2 diffusion process in agarose gel was obtained using the MSF at different time points after H_2O_2 was added to the surface of the gel; two technical repeats were performed. **c**, Photographs of a nude mouse with tumour tissue, into which we injected an MSF (top). Bottom, a magnification of the area indicated by a dashed red box in the top image. Scale bars, 1 cm (top) and 3 mm (bottom). **d**, A PA image of tumour tissue that was injected with an MSF; the longest fibre reaches the centre of the tumour. Scale bar, 1 mm. **e**, Mapping of the spatial and temporal distribution of H_2O_2 in a mature tumour with a volume of 1,950 mm^3 over 20 h in vivo. **f**, A graph showing the distribution of H_2O_2 inside six tumours with a volume of 80 mm^3 to 1,283 mm^3 during growth. As the tumour increases in volume, the distribution of H_2O_2 changes accordingly, with higher H_2O_2 concentrations in the centre of the larger tumour. Each Gaussian simulation was performed on the basis of five experimental data points from one tumour. The boundaries of the tumours were then outlined on the simulated gradient map. **g**, Photographs showing typical dissected tumour tissues, with sizes ranging from 80 mm^3 to 1,283 mm^3 , that were obtained after the in vivo MSF measurement described in **f**; six technical repeats were performed. Scale bar, 1 cm.

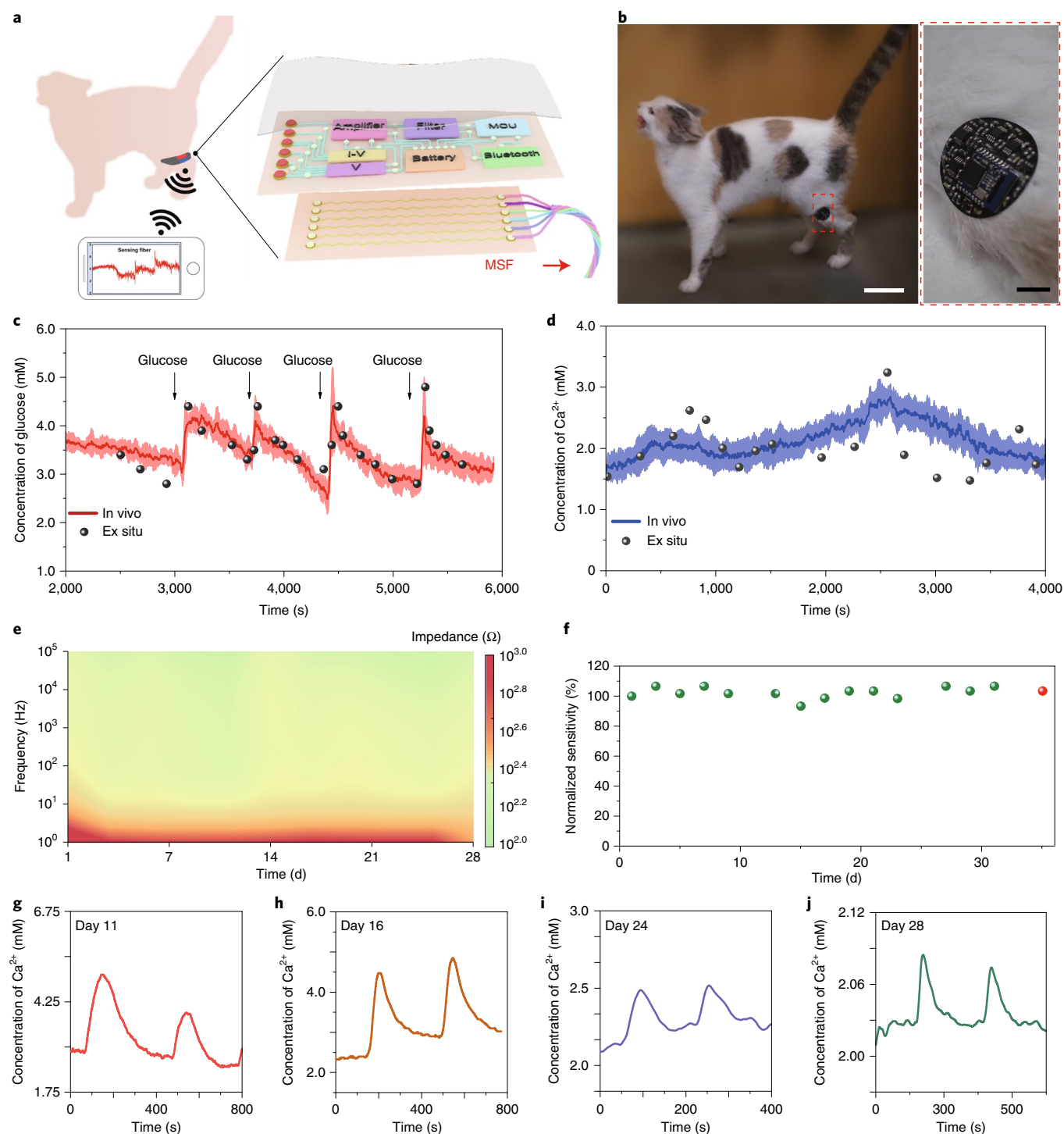


Fig. 6 | The use of MSFs for real-time and long-term multiplex monitoring in vivo. **a**, Schematic of the integrated system for wireless transmission of transformed glucose signals from an implanted MSF. **b**, Photographs of a cat wearing a 'smart wristband' during real-time monitoring. The flexible patch conforms well to skin. Scale bars, 6 cm (left) and 6 mm (right). **c, d**, Comparison between ex situ calibration data for glucose (**c**) and Ca^{2+} (**d**) from collected blood samples and on-body readings, from the integrated system using an MSF, during real-time monitoring. **e**, The impedance magnitude of Ca^{2+} SSFs remains stable in the vein of a cat during implantation for 28 d. **f**, The stable sensitivity of Ca^{2+} SSFs in vitro for 28 d (green dots). Another Ca^{2+} SSF was implanted into a cat vein for 28 d and then tested in vitro (red dot). The red dot showed no obvious difference compared with the green dots, indicating stable sensitivity in vivo. Three technical repeats were performed. **g-j**, In vivo detection of Ca^{2+} using a Ca^{2+} SSF on different days during a 28 d period. Three technical repeats were performed. This test was performed in three cats, and the stability remained. A typical example is shown above.

conducted electrochemical tests in a mature solid tumour with a volume of $1,950 \text{ mm}^3$ every 4 h and mapped the spatial and temporal distribution of H_2O_2 (Fig. 5e). The concentration of H_2O_2 decreased stepwise from the inside out at gradients of about $143 \mu\text{M}$, $101 \mu\text{M}$,

$74 \mu\text{M}$, $54 \mu\text{M}$ and $22 \mu\text{M}$. The increasing levels of H_2O_2 towards the centre of the tumour probably follows the decreasing gradient of oxygen supply in mature tumours³¹. The concentration of H_2O_2 inside the tumour was nearly $120 \mu\text{M}$ higher than the outside, with

only small fluctuations over 20 h. To understand how tumours reach homeostasis in response to rapid changes in the microenvironment, we further studied the distribution of H_2O_2 inside the tumour at different stages of growth. As the tumour volume varied from 80 mm^3 to $1,283\text{ mm}^3$ during growth, the patch distance of SSFs in an MSF was designed from $150\text{ }\mu\text{m}$ to 1 mm and the concentration of H_2O_2 at the central position increased from $16\text{ }\mu\text{M}$ to $98\text{ }\mu\text{M}$ (Fig. 5f,g). The distribution of H_2O_2 changed from being uniform to a gradient along with tumour growth and gradually appeared to decrease from the inside out. By correlating the spatial gradient of H_2O_2 and other chemicals, such as O_2 and pH, with hypoxic gradients in cancerous tumours, it is possible to understand tumorigenesis, tumour development and how tumours survive hypoxia.

MSFs as real-time and long-term multiplex sensors in vivo

For diseases such as type 1 diabetes that require real-time monitoring and feedback, the MSF together with implantation offers an effective method for monitoring relevant analytes and delivering therapy on time without the need for additional equipment³⁹. To test this, we integrated the injected MSF (the sensing component) with the signal transduction, conditioning, processing and wireless transmission paths on a flexible stretchable polymer patch that conformed and adhered well to the body (Fig. 6a,b). Data from the patch were transmitted wirelessly to a Bluetooth-enabled mobile handset (the circuit design, calibration and power diagram of the integrated system are provided in the Methods and Supplementary Figs. 34 and 35). When tested on a conscious cat, electrochemical signals based on both current-mode (glucose sensor) and voltage-mode (ion sensor) devices were obtained (Fig. 6b, Supplementary Video 1). The real-time electrochemical data that were obtained from the patch by injecting the cat with glucose four times matched well with ex situ measurements of blood samples (Fig. 6c, black data points). The blood calcium fluctuations ($2.0\text{--}2.8\text{ mM}$) were also observed (Fig. 6d). These results show that electrochemical readings from MSFs are accurate and timely, offering a monitoring tool that is free from complex sampling procedures and cumbersome equipment.

The MSF was retained in behaving cats for 28 d to verify its potential for long-term application in vivo. The impedance magnitude of Ca^{2+} SSFs remained stable throughout the continuous monitoring (Fig. 6e). The sensitivity was stable during an in vitro test for more than 28 d (Fig. 6f). The implanted Ca^{2+} SSFs were able to monitor changes in Ca^{2+} levels in cats for 28 d (Fig. 6g–j). Finally, the Ca^{2+} SSF was removed after chronic in vivo implantation, and the sensitivity was also found to be well maintained compared with the in vitro test (Fig. 6f). The scanning electron microscope (SEM) images demonstrated that the surface of the SSF was well preserved (Supplementary Fig. 36), which accommodated its long-term electrochemical stability. Furthermore, the ZnO-based glucose SSFs also remained stable and effective over continuous testing in vitro and monitoring in vivo for 28 d (Supplementary Figs. 37 and 38). These results indicate a promising route to benefit patients with real-time health monitoring at a low cost and a low level of discomfort in the future.

In summary, we have introduced a flexible fibre-based implantable sensor that mimics the hierarchical and helical assembly and mechanical properties of native soft tissues. The sensor was made by twisting CNTs into hierarchical and helical bundles of fibres. When injected into tissue using a syringe, the sensor formed a stable fibre-tissue interface and showed good biointegration, offering a robust tool for long-term sensing applications. MSFs with axial or radial distributions of terminals enabled the simultaneous detection of multiple-target analytes with spatially resolved and real-time feedback. We showed real-time monitoring of H_2O_2 in solid tumours and Ca^{2+} and glucose concentrations in blood vessels. By creating a library of SSFs with different sensing functionalities, it is possible to obtain an unlimited number of combinations of sensing elements,

offering an important opportunity for discovering and understanding the mechanisms of various diseases. Furthermore, we integrated the sensing fibres with a wirelessly transmitting device, and enabled portable and convenient monitoring of physiological information.

Methods

Fabrication of SSFs. All of the SSFs were fabricated by decorating analyte sensitive components onto CNT fibres and insulating the fibre with a thin layer of PDMS. A detailed description of the preparation of the CNT fibre is provided in the Supplementary Information. Details of the modification method for individual SSFs are provided below.

Fabrication of H_2O_2 SSFs. The H_2O_2 SSFs were prepared by depositing Pt nanoparticles onto a CNT fibre using an electrochemical double potential step method. A KCl (0.1 M, Sinopharm) and K_2PtCl_6 (1 mM, Sigma) aqueous solution was used as the electrolyte, and CNT fibre, Pt wire (Shanghai Yueci) and Ag/AgCl (Shanghai Yueci) were used as the working, counter and reference electrodes, respectively. In a typical electrochemical cycle, the deposition was conducted by setting the first step at 0.5 V for 10 s and the second step at -0.7 V for 10 s. The Pt–CNT composite fibre was obtained after 50 cycles.

Fabrication of glucose SSFs. A multi-step electrochemical procedure was used to fabricate glucose SSFs⁴⁰. The glucose SSFs were classified into two typical categories—enzyme-based glucose SSFs and ZnO-based glucose SSFs. For the enzyme-based type, PANI was first deposited onto the fibre as an electron-transport layer to widen the linear range using a chronoamperometry method at 0.75 V for 20 s. Aqueous solution of 0.5 M aniline (Sinopharm) and 1 M H_2SO_4 (Sinopharm) was used as electrolyte and Pt wire and Ag/AgCl were used as the counter and reference electrodes, respectively. Second, Pt nanoparticles were deposited onto the PANI/CNT fibre, as described for the preparation of H_2O_2 SSFs. Third, the fibre was coated with a glucose-responsive layer. Chitosan (Aladdin) solution of 1 wt% was prepared by dissolving chitosan in 2 wt% acetic acid (Sinopharm) aqueous solution under magnetic stirring for about 1 h, and it was then mixed with single-wall CNTs (2 mg ml^{-1} , Aladdin) under ultrasonic agitation. Glucose oxidase (GOx; 40 mg ml^{-1} , Aladdin) was then added. The Pt/PANI/CNT fibre with a length of $500\text{ }\mu\text{m}$ was dip-coated with the mixed solution ($4\text{ }\mu\text{l}$) to obtain a GOx/Pt/PANI/CNT fibre. After drying at room temperature, the GOx/Pt/PANI/CNT fibre was dip-coated with Nafion aqueous solution ($2\text{ }\mu\text{l}$, 0.5 wt%, Sigma). Finally, the electrode was immersed in glutaraldehyde (2 wt%, Aladdin) aqueous solution for 30 min, in which Nafion film was crosslinked by glutaraldehyde with micropores, which enhances the selectivity and broadens the linear range. The glucose SSFs were obtained after drying overnight at $4\text{ }^\circ\text{C}$ in the dark. For ZnO-based glucose SSFs⁴¹, ZnO nanoparticles (Aladdin, 0.24 g) and MWCNT-COOH (Sigma, 0.08 g) were dissolved in a mixture of 10 ml water and 15 ml ethylene glycol, dispersed by ultrasonic treatment and stirred for 20 h at $80\text{ }^\circ\text{C}$. The resulting product was washed with water and ethanol and dried at $60\text{ }^\circ\text{C}$. Then, 0.05 g of dried product was dispersed in dimethylformamide mixed with 5% Nafion aqueous solution (3/1, v/v) and stirred for 24 h. The CNT fibre was dip-coated with the obtained mixture ($3\text{ }\mu\text{l}$), and ZnO-based glucose SSFs were obtained after drying at $50\text{ }^\circ\text{C}$.

Fabrication of SSFs for ions (Ca^{2+} , K^+ , Na^+ and H^+). For Ca^{2+} SSFs, PEDOT:PSS and a Ca^{2+} -selective membrane cocktail were coated onto the CNT fibre to prepare Ca^{2+} SSFs. First, PEDOT:PSS aqueous solution (Heraeus, AL4083) was coated onto the CNT fibre three times to obtain PEDOT:PSS/CNT fibres. Second, calcium ionophore II (1% by weight, w/w, Sigma), sodium tetraphenylborate (0.55% w/w, Sigma), polyvinyl chloride (33% w/w, Sigma) and bis(2-ethylehexyl) sebacate (65.45% w/w, Aladdin) were mixed to prepare the Ca^{2+} -selective cocktail. Third, 100 mg of the membrane cocktail was dissolved in $660\text{ }\mu\text{l}$ of tetrahydrofuran (Aladdin). One PEDOT:PSS/CNT fibre was dipped into the solution and a uniform coating was obtained. The Ca^{2+} SSFs were finally dried overnight at $4\text{ }^\circ\text{C}$ in the dark. For Na^+ SSFs³², a Na^+ -selective membrane cocktail was prepared by mixing Na ionophore X (1% by weight, w/w, Sigma), Na-TFPB (0.55% w/w, Sigma), polyvinyl chloride (33% w/w, Sigma) and bis(2-ethylehexyl) sebacate (65.45% w/w, Aladdin). Then, 100 mg of the Na^+ -selective membrane cocktail was dissolved in $660\text{ }\mu\text{l}$ of tetrahydrofuran (Aladdin). For K^+ SSFs, a K^+ -selective membrane cocktail was generated by mixing valinomycin (2% by weight, w/w, Sigma), sodium tetraphenylborate (0.5% w/w, Sigma), polyvinyl chloride (32.7% w/w, Sigma) and bis(2-ethylehexyl) sebacate (64.7% w/w, Aladdin). Then 100 mg of the K^+ -selective membrane cocktail was dissolved in $350\text{ }\mu\text{l}$ of cyclohexanone (Aladdin). The other steps were the same as Ca^{2+} SSFs. For pH SSFs, a solution of 0.1 M aniline/0.1 M H_2SO_4 was prepared and the pH SSFs were fabricated in the mixed solution by cyclic voltammetry from -0.2 to 1 V for 25 cycles at 100 mV s^{-1} .

Fabrication of PSA SSFs. A simple amperometric peptide-based PSA SSF was developed⁴². First, a poly(diallyldimethylammonium chloride) (PDDA)–graphene oxide (GO) solution was generated as follows: PDDA ($114\text{ }\mu\text{l}$, 35% w/w, Sigma) aqueous solution, 1.169 g NaCl (Sinopharm) and GO aqueous solution (20 ml,

0.5 g l⁻¹) were mixed, centrifuged and dissolved in 10 ml water. Second, chitosan solution (0.1 wt%) was prepared and mixed with K₄[Fe(CN)₆] (10 µl, 0.5 wt%, Sinopharm) aqueous solution, 60 µl PDDA-GO solution and 1.120 ml water. Third, CNT fibre was dipped in the mixture 20 times, once every 3 min. After drying, the fibre was immersed in the mixture of glutaraldehyde (0.05 wt%) and Pb(NO₃)₂ (0.1 M, Aladdin) for 30 min and then washed three times with water. The resulting fibre was then immersed in 1 wt% glutaraldehyde for 30 min and washed three times with water. Finally, peptide (0.2 mg ml⁻¹, Solarbio) was mixed with albumin to prepare bovine serum (0.01 mg ml⁻¹, Sigma) aqueous solution and the fibre was immersed in the solution for 1 h. After drying overnight at 4 °C in the dark, one PSA SSF was obtained.

Fabrication of the reference electrode. The Ag/AgCl reference electrode was prepared using a cyclic voltammetry method. First, the CNT fibre was immersed in a mixed aqueous solution consisting of 5 mM AgNO₃ and 1 M KNO₃ by sweeping from -0.9 to 0.9 V for 7 cycles at a scan rate of 0.1 V s⁻¹, with a two-electrode system, in which the CNT fibre acted as working electrode and a commercial silver electrode (Shanghai Yueci) served as both the counter and reference electrode. Second, the Ag/CNT fibre was dipped into an aqueous solution of 0.1 M KCl and 0.01 M HCl by sweeping from -0.15 to 1.05 V for 2 cycles at a scan rate of 0.05 V s⁻¹ with a commercial Ag/AgCl electrode as both the counter and reference electrode. The Ag/AgCl reference fibre electrode was obtained after drying. The Ag/AgCl reference fibre electrode was next coated with a polymer layer based on Nafion/glutaraldehyde aqueous solution before being implanted.

Fabrication of MSFs. The structure of MSFs for spatial analysis and multiplex monitoring was demonstrated using the Ag/AgCl fibre electrode as the core and five H₂O₂ SSFs were uniformly arranged along the axial direction or around the core⁴³. First, five H₂O₂ SSFs were arranged in parallel with space of 50 µm. The ends of functional SSFs were cut into a wedge with an angle of θ from the reference electrode, which was determined by the desired pitch distance of the MSF. For the multiplex monitoring fibre, θ was set as zero. The arranged fibre end was then fixed onto a rotating motor shaft and the other end was fixed by adhesive tape. The motor was operated at a speed of 200 rad min⁻¹ for about 10 s to deliver an MSF.

Animals. Ten female and three male adult cats (*Felis catus*, about 1.5–2.5 kg in weight, aged from one to two years old) were purchased from Shanghai Yingen Farm. Seven-week-old BALB/c nude mice (female, about 20 g in weight) were purchased from the Shanghai SLAC Laboratory Animal Co. The experimental protocols were approved by the Animal Experimentation Committee of Fudan University. All of the animals were treated in accordance with guidelines for the care and use of experimental animals described by the National Institutes of Health and Fudan University.

Biocompatibility of the fibres. Cats were euthanized by lethal injection after all of the materials had been implanted for 5 d, 21 d or 35 d. Tissues containing fibres were incised into small blocks (about 1 cm × 1 cm × 0.5 cm) and fixed with 4% (v/v) paraformaldehyde in 1 × PBS solution at 4 °C and sliced into sections with a thickness of about 4 µm using a microtome (Leica RM 2135, Leica Microsystems). Next, H&E staining, Masson's trichrome staining and immunohistochemical (IHC) staining of CD11b were conducted according to a standard procedure, which is described in the Supplementary Information. Typically, a H&E Staining Kit (C0105, Beyotime Institute of Biology) and a Masson's Trichrome Staining Kit (G1006, Servicebio) were used. Corresponding sections were mounted with neutral resins and observed under a microscope (Nikon Alphaphot-2). For IHC staining, antigen retrieval was performed by heating in 0.01 M citrate buffer (pH 6.0) for 10 min at medium heat of a microwave oven (~400 W) and another 7 min at medium-low heat of a microwave oven (~240 W) after a break for 10 min. Anti-CD11b antibodies (1:300, ab133357, Abcam) were used as primary antibodies and Cy3-conjugated goat anti-rabbit IgG (H + L) (1:300, GB21303, Servicebio) was used as secondary antibody. IHC sections were mounted with DAPI Fluoromount-G (0100-20, Southern Biotech) and observed using a confocal microscope.

Fabrication of the wireless integrated system. The conditioning path for each SSF was implemented in relation to the corresponding sensing mode. In the case of the amperometric-based glucose and H₂O₂ SSFs, the originally generated signal was collected in the form of an electrical current. A transimpedance amplifier was therefore used to convert the signal current into voltage. In the case of the Ca²⁺ SSFs, the generated signals were essentially the voltage differences between the Ag/AgCl reference electrode and the working electrode of Ca²⁺ SSF. We therefore measured the difference in potential of the Ca²⁺ SSF and Ag/AgCl electrode directly. The details of the conditioning path for each SSF and the whole circuit consisting of conditioning path, amplifier, filter, Bluetooth module and user interface are included in the Supplementary Information. A mobile application was designed to accompany the integrated system and to provide a user interface for data collection. After the MSF injection, conductive silver paint was coated between the device and the circuit.

The use of MSFs to detect the spatial gradient of H₂O₂ in a mouse tumour. Seven-week-old female mice with subcutaneous tumours of different sizes from

80 mm³ to 1,950 mm³ were chosen as the experimental animals. To detect the distribution of H₂O₂ during tumour growth, the first day of the test started with a tumour size of 80 mm³, and the tumour size and the distribution of H₂O₂ were tested every 3 d. The MSF for spatial analysis was injected into the tumour tissue of a nude mouse. Each SSF was covered by conductive silver paint, connected to the circuit and tested in chronoamperometry at -0.42 V. The distribution of H₂O₂ in mature tumours was tested every 4 h for over 20 h.

The simulation of the concentration was acquired by two-dimensional Gaussian fitting on the basis of experimental data. The centre of each tumour was defined from the optical photographs. In the simulation, we assumed that dots with the same distances from their centres should have the same simulated concentration of H₂O₂, so the fitting function we used was listed as follows:

$$f(x, y) = \frac{1}{2\pi\sigma^2} \exp\left[-\frac{1}{2\sigma^2}((x - \mu_1)^2 + (y - \mu_2)^2)\right]$$

where σ is the s.d. of the Gaussian fitting, x and y are the coordinates of the dot, and μ_1 and μ_2 are the coordinates of the centre.

MSF as a real-time and long-term multiplex sensor in vivo. Five adult cats (1.5–2.5 kg) were used as the experimental animals. MSFs prepared from Ca²⁺ and glucose fibre with an Ag/AgCl electrode as the reference electrode were prepared. The MSF was injected into the femoral vein for continuous monitoring. Different doses of glucose and sodium chloride solution, and calcium and sodium chloride solution (100 mM CaCl₂ and 154 mM NaCl solution) were injected into another femoral vein of the animal to raise the blood glucose and calcium level, respectively. Each test was performed for more than 2 h. The Ca²⁺ SSFs and ZnO-based glucose SSFs were tested in vivo for 28 d.

Verification of the fidelity of the sensors in vivo. To prove the accuracy of the test, the blood glucose of the cats were measured using a commercial glucose meter (On Call EZ2, ACON Biotech) and the blood calcium was measured using a commercial calcium assay kit (K380-250, Biovision). Both blood samples were collected from the auricular veins of the cats using a blood lancet. The level of blood glucose was measured during the test by dipping blood samples into the reaction groove, and data were exported immediately. Blood samples for the blood calcium tests were collected during the test by dipping the blood (10 µl) into a heparin-treated Eppendorf tube. After the test was completed, a commercial calcium assay kit was used to measure the level of calcium in the blood sample by spectrophotometry. The blood samples (10 µl) were diluted with 40 µl distilled water and then mixed with 90 µl chromogenic reagent and 60 µl calcium assay buffer, and then the mixture was left to stand for 10 min. The optical density at 575 nm was measured using a NanoDrop 8000. The calibration curve was acquired using the standard sample in the kit. The blood samples were stored at 4 °C between the test and measurement.

Calculation of bending stiffness. To calculate the bending stiffness (D), a fixed boundary was set as one of the ends parallel with the bending direction, and a small vertical displacement, d , was added on the end. The bending stiffness can be defined as

$$D = EI$$

where E and I are the elastic modulus and moment of inertia, respectively.

For a beam with a rectangular cross-section with width b and height h , the moment of inertia is

$$I = \frac{bh^3}{12}$$

For a circular cross-section of diameter d , the moment of inertia is

$$I = \frac{\pi d^4}{64}$$

von Mises stress simulation of assembled fibres under compression. Although the CNTs were based on nanoscale, the laws of continuum mechanics were still robust and applicable^{44,45}. Moreover, when the aspect ratio of fibres was relatively larger, the CNTs could be treated as simple continuum beam models^{46–48}, which substantially reduces the computation cost efficiency compared with atomistic models.

Parallel-arranged, non-sliding fibres were considered to simplify the hierarchical model⁴⁹. To explain how the structure of the CNT fibres affects their macroscopic properties, we applied finite element method using the software ABAQUS (Analysis Users Manual, version 6.13, 2013) to simulate the deformation of CNT fibres with the length $L = 25 \mu\text{m}$ and the diameter of cross-section $d = 50 \text{ nm}$. The elastic modulus and Poisson's ratio of CNT were 1 TPa and 0.3, respectively. Van der Waals interactions played a key role between two CNTs^{44–47}, and Tang et al.⁵⁰ previously predicted that the equilibrium separation between two parallel CNTs is 3.5 Å. For different hierarchical CNT bundles, we defined the void ratio of cross-section as the void area over the entire cross-sectional area.

In the simulation, beam elements (B31) were applied to discretize the CNT bundles. Inspired by previous work by Huang et al.³¹, we used spring elements to represent the van der Waals interactions. Considering both axial and radial van der Waals interplay, oblique distributed linear springs were used in the interaction between adjacent CNTs. Taking the Hamaker constant $A = 10^{-19}$ J as a typical value, the van der Waals energy of parallel cylinders or rods of radii R_1 and R_2 (per unit length) can be expressed as³²:

$$W = \frac{-A}{12\sqrt{2}X^{3/2}} \left(\frac{R_1 R_2}{R_1 + R_2} \right)^{1/2}$$

which leads to the van der Waals force:

$$F = -\frac{dW}{dX} = \frac{-A}{8\sqrt{2}X^{5/2}} \left(\frac{R_1 R_2}{R_1 + R_2} \right)^{1/2}$$

where X denotes a distance between separated surfaces and F' denotes the derivative of the van der Waals force with respect to X . Considering the first two terms of its Taylor series expanded at the initial distance X_0 , we obtained

$$\begin{aligned} F(X) &\approx F(X_0) + F'(X_0) \cdot (X - X_0) \\ &\approx F(X_0) + \left(\frac{5A}{16\sqrt{2}} \left(\frac{R_1 R_2}{R_1 + R_2} \right)^{1/2} X_0^{-7/2} \right) \cdot (X - X_0) \end{aligned}$$

By analogy with the classical spring model:

$$F_2 - F_1 = k \cdot (x_2 - x_1)$$

we have

$$k \approx \left(\frac{5A}{16\sqrt{2}} \left(\frac{R_1 R_2}{R_1 + R_2} \right)^{1/2} X_0^{-7/2} \right)$$

where k denotes the spring stiffness.

When subjected to axial compression, the CNT fibre may undergo a nonlinear buckling response. To predict the buckling behaviour of CNT fibres, Riks algorithm was adopted to obtain nonlinear equilibrium solutions for the overall buckling process of CNT fibres.

von Mises stress simulation of fibres embedded in tissues. The fibres implanted into the tissue deform with the vicinity under different loads. Considering the practical applications, excessive stress on the interface between two materials may cause damage and even tearing of tissue. To study the deformation at the interface and to predict the stress distribution, we established finite element models with various geometries and loads.

To solve large deformations of fibre-embedded tissues, a pseudo-dynamic algorithm (a stabilized nonlinear resolution method in finite element software ABAQUS) was used for two types of loading—twisting and bending. In the simulation, the elastic modulus and Poisson's ratio of medium are 480 MPa and 0.3, respectively, which are equivalent to the muscle⁹. For a comprehensive analysis, we choose different types of fibre to implant into the medium, including CNT fibre (elastic modulus, 2.0 GPa; Poisson's ratio, 0.3), CF (elastic modulus, 290 GPa; Poisson's ratio, 0.3), tungsten wire (elastic modulus, 400 GPa; Poisson's ratio, 0.28) and gold wire (elastic modulus, 77 GPa; Poisson's ratio, 0.42). The diameter of the fibres is 50 μ m, and the length is 10 mm. Widely used polymer films were taken into account, including PET (elastic modulus, 2.6 GPa; Poisson's ratio, 0.4) and PI (elastic modulus, 23 GPa; Poisson's ratio, 0.33) with thickness of 50 μ m, width of 5 mm and length of 10 mm.

Reporting Summary. Further information on research design is available in the Nature Research Reporting Summary linked to this article.

Data availability

The main data supporting the results in this study are available within the paper and its Supplementary Information. The raw and analysed datasets that were generated during this study are available from the corresponding authors on reasonable request.

Received: 30 October 2018; Accepted: 12 September 2019;

Published online: 28 October 2019

References

- Clausen, J. Man, machine and in between. *Nature* **457**, 1080–1081 (2009).
- Yoshida Kozai, T. D. et al. Ultrasmall implantable composite microelectrodes with bioactive surfaces for chronic neural interfaces. *Nat. Mater.* **11**, 1065–1073 (2012).
- Canales, A. et al. Multifunctional fibers for simultaneous optical, electrical and chemical interrogation of neural circuits in vivo. *Nat. Biotechnol.* **33**, 277–284 (2015).
- Jun, J. J. et al. Fully integrated silicon probes for high-density recording of neural activity. *Nature* **551**, 232–236 (2017).
- Yun, S. H. & Kwok, S. J. J. Light in diagnosis, therapy and surgery. *Nat. Biomed. Eng.* **1**, 0008 (2017).
- Mineev, I. R. et al. Electronic dura mater for long-term multimodal neural interfaces. *Science* **347**, 159–163 (2015).
- An, D. et al. Designing a retrievable and scalable cell encapsulation device for potential treatment of type 1 diabetes. *Proc. Natl Acad. Sci. USA* **115**, E263–E272 (2018).
- Vermesh, O. et al. An intravascular magnetic wire for the high-throughput retrieval of circulating tumour cells in vivo. *Nat. Biomed. Eng.* **2**, 696–705 (2018).
- Feiner, R. & Dvir, T. Tissue–electronics interfaces: from implantable devices to engineered tissues. *Nat. Rev. Mater.* **3**, 17076 (2017).
- Yu, X. et al. Needle-shaped ultrathin piezoelectric microsystem for guided tissue targeting via mechanical sensing. *Nat. Biomed. Eng.* **2**, 165–172 (2018).
- Lacour, S. P., Courtine, G. & Guck, J. Materials and technologies for soft implantable neuroprostheses. *Nat. Rev. Mater.* **1**, 16063 (2016).
- Chen, R., Canales, A. & Anikeeva, P. Neural recording and modulation technologies. *Nat. Rev. Mater.* **2**, 16093 (2017).
- Hong, G. & Lieber, C. M. Novel electrode technologies for neural recordings. *Nat. Rev. Neurosci.* **20**, 330–345 (2019).
- Yang, X. et al. Bioinspired neuron-like electronics. *Nat. Mater.* **18**, 510–517 (2019).
- Ling, S., Kaplan, D. L. & Buehler, M. J. Nanofibrils in nature and materials engineering. *Nat. Rev. Mater.* **3**, 18016 (2018).
- Buehler, M. J. Nature designs tough collagen: explaining the nanostructure of collagen fibrils. *Proc. Natl Acad. Sci. USA* **103**, 12285–12290 (2006).
- Hang, F. & Barber, A. H. Nano-mechanical properties of individual mineralized collagen fibrils from bone tissue. *J. R. Soc. Interface* **8**, 500–505 (2011).
- Depalle, B., Qin, Z., Shefelbine, S. J. & Buehler, M. J. Influence of cross-link structure, density and mechanical properties in the mesoscale deformation mechanisms of collagen fibrils. *J. Mech. Behav. Biomed. Mater.* **52**, 1–13 (2015).
- Dai, X., Hong, G., Gao, T. & Lieber, C. M. Mesh nanoelectronics: seamless integration of electronics with tissues. *Acc. Chem. Res.* **51**, 309–318 (2018).
- Darnell, M. & Mooney, D. J. Leveraging advances in biology to design biomaterials. *Nat. Mater.* **16**, 1178–1184 (2017).
- Baker, B. M. et al. Cell-mediated fibre recruitment drives extracellular matrix mechanosensing in engineered fibrillar microenvironments. *Nat. Mater.* **14**, 1262–1268 (2015).
- Waldert, S. Invasive vs. non-invasive neuronal signals for brain–machine interfaces: will one prevail? *Front. Neurosci.* **10**, 295 (2016).
- Vitale, F. et al. Fluidic microactuation of flexible electrodes for neural recording. *Nano Lett.* **18**, 326–335 (2018).
- Liu, J. et al. Syringe-injectable electronics. *Nat. Nanotechnol.* **10**, 629–636 (2015).
- Close, R. I. Dynamic properties of mammalian skeletal muscles. *Physiol. Rev.* **52**, 129–197 (1972).
- Alonso, J. L. & Goldmann, W. H. Feeling the forces: atomic force microscopy in cell biology. *Life Sci.* **72**, 2553–2560 (2003).
- Liu, Y., Zhao, Y., Sun, B. & Chen, C. Understanding the toxicity of carbon nanotubes. *Acc. Chem. Res.* **46**, 702–713 (2013).
- Jhunjhunwala, S. et al. Neutrophil responses to sterile implant materials. *PLoS ONE* **10**, e0137550 (2015).
- Gurtner, G. C., Werner, S., Barrandon, Y. & Longaker, M. T. Wound repair and regeneration. *Nature* **453**, 314–321 (2008).
- Yang, Z. et al. Recent advancement of nanostructured carbon for energy applications. *Chem. Rev.* **115**, 5159–5223 (2015).
- D'Amico, A. V., Chen, M.-H., Roehl, K. A. & Catalona, W. J. Preoperative PSA velocity and the risk of death from prostate cancer after radical prostatectomy. *N. Engl. J. Med.* **351**, 125–135 (2004).
- Gao, W. et al. Fully integrated wearable sensor arrays for multiplexed in situ perspiration analysis. *Nature* **529**, 509–514 (2016).
- Zhu, S., Nih, L., Carmichael, S. T., Lu, Y. & Segura, T. Enzyme-responsive delivery of multiple proteins with spatiotemporal control. *Adv. Mater.* **27**, 3620–3625 (2015).
- Oxley, T. J. et al. Minimally invasive endovascular stent-electrode array for high-fidelity, chronic recordings of cortical neural activity. *Nat. Biotechnol.* **34**, 320–327 (2016).
- Luo, Y., Liu, H., Rui, Q. & Tian, Y. Detection of extracellular H₂O₂ released from human liver cancer cells based on TiO₂ nanoneedles with enhanced electron transfer of cytochrome *c*. *Anal. Chem.* **81**, 3035–3041 (2009).
- Rodenhizer, D. et al. A three-dimensional engineered tumour for spatial snapshot analysis of cell metabolism and phenotype in hypoxic gradients. *Nat. Mater.* **15**, 227–234 (2016).

37. Chen, Q. et al. H₂O₂-responsive liposomal nanoprobe for photoacoustic inflammation imaging and tumor theranostics via in vivo chromogenic assay. *Proc. Natl Acad. Sci. USA* **114**, 5343–5348 (2017).
38. Hong, G., Antaris, A. L. & Dai, H. Near-infrared fluorophores for biomedical imaging. *Nat. Biomed. Eng.* **1**, 0010 (2017).
39. Lipani, L. et al. Non-invasive, transdermal, path-selective and specific glucose monitoring via a graphene-based platform. *Nat. Nanotechnol.* **13**, 504–511 (2018).
40. Lee, H. et al. Wearable/disposable sweat-based glucose monitoring device with multistage transdermal drug delivery module. *Sci. Adv.* **3**, e1601314 (2017).
41. Tarlani, A. et al. New ZnO nanostructures as non-enzymatic glucose biosensors. *Biosens. Bioelectron.* **67**, 601–607 (2015).
42. Tang, Z., Fu, Y. & Ma, Z. Bovine serum albumin as an effective sensitivity enhancer for peptide-based amperometric biosensor for ultrasensitive detection of prostate specific antigen. *Biosens. Bioelectron.* **94**, 394–399 (2017).
43. Chen, P. et al. Hierarchically arranged helical fibre actuators driven by solvents and vapours. *Nat. Nanotechnol.* **10**, 1077–1083 (2015).
44. He, X. Q. et al. Buckling analysis of multi-walled carbon nanotubes: a continuum model accounting for van der Waals interaction. *J. Mech. Phys. Solids* **53**, 303–326 (2005).
45. Ru, C. Q. Effect of van der Waals forces on axial buckling of a double-walled carbon nanotube. *J. Appl. Phys.* **87**, 7227–7231 (2000).
46. Natsuki, T. et al. Stability analysis of double-walled carbon nanotubes as AFM probes based on a continuum model. *Carbon* **49**, 2532–2537 (2011).
47. Timesli, A. et al. Prediction of the critical buckling load of multi-walled carbon nanotubes under axial compression. *C. R. Mec.* **345**, 158–168 (2017).
48. Khosravian, N. & Rafii-Tabar, H. Computational modelling of a non-viscous fluid flow in a multi-walled carbon nanotube modelled as a Timoshenko beam. *Nanotechnology* **19**, 275703 (2008).
49. Sun, H. et al. Energy harvesting and storage in 1D devices. *Nat. Rev. Mater.* **2**, 17023 (2017).
50. Tang, T. et al. Adhesion between single-walled carbon nanotubes. *J. Appl. Phys.* **97**, 074304 (2005).
51. Huang, S. Q. et al. Pattern instability of a soft elastic thin film under van der Waals forces. *Mech. Mater.* **38**, 88–99 (2006).
52. Israelachvili, J. N. *Intermolecular and Surface Forces* (Academic, 2011).

Acknowledgements

We thank A. L. Chun of Science Storylab for her suggestions and critique; F. Han from Fudan University for help with the wireless-transmitting system. This work was supported by MOST (grant number 2016YFA0203302), NSFC (grant numbers 21634003, 51573027, 51673043, 21604012, 21805044, 21875042, 11602058 and 11872150), STCSM (grant numbers 16JC1400702, 17QA1400400, 18QA1400700, 18QA1400800 and 19QA1400500), SHMEC (grant number 2017-01-07-00-07-E00062), SEDF (grant number 16CG01) and Yanchang Petroleum Group and China Postdoctoral Science Foundation (grant numbers 2017M610223 and 2018T110334). This work was also supported by Shanghai Municipal Science and Technology Major Project (2018SHZDZX01) and ZJLab (to H.Y.).

Author contributions

X.S., F.X., H.Y. and H.P. conceived and designed the research project. L.W., Z.W. and S.X. performed the experiments. F.L. and Y.Y. performed numerical simulations. L.W., S.X. and Z.W. analysed the data. All of the authors discussed the data and wrote the paper.

Competing interests

The authors declare no competing interests.

Additional information

Supplementary information is available for this paper at <https://doi.org/10.1038/s41551-019-0462-8>.

Correspondence and requests for materials should be addressed to X.S., F.X., H.Y. or H.P.

Reprints and permissions information is available at www.nature.com/reprints.

Publisher's note Springer Nature remains neutral with regard to jurisdictional claims in published maps and institutional affiliations.

© The Author(s), under exclusive licence to Springer Nature Limited 2019

Reporting Summary

Nature Research wishes to improve the reproducibility of the work that we publish. This form provides structure for consistency and transparency in reporting. For further information on Nature Research policies, see [Authors & Referees](#) and the [Editorial Policy Checklist](#).

Statistics

For all statistical analyses, confirm that the following items are present in the figure legend, table legend, main text, or Methods section.

n/a Confirmed

- The exact sample size (n) for each experimental group/condition, given as a discrete number and unit of measurement
- A statement on whether measurements were taken from distinct samples or whether the same sample was measured repeatedly
- The statistical test(s) used AND whether they are one- or two-sided
Only common tests should be described solely by name; describe more complex techniques in the Methods section.
- A description of all covariates tested
- A description of any assumptions or corrections, such as tests of normality and adjustment for multiple comparisons
- A full description of the statistical parameters including central tendency (e.g. means) or other basic estimates (e.g. regression coefficient) AND variation (e.g. standard deviation) or associated estimates of uncertainty (e.g. confidence intervals)
- For null hypothesis testing, the test statistic (e.g. F , t , r) with confidence intervals, effect sizes, degrees of freedom and P value noted
Give P values as exact values whenever suitable.
- For Bayesian analysis, information on the choice of priors and Markov chain Monte Carlo settings
- For hierarchical and complex designs, identification of the appropriate level for tests and full reporting of outcomes
- Estimates of effect sizes (e.g. Cohen's d , Pearson's r), indicating how they were calculated

Our web collection on [statistics for biologists](#) contains articles on many of the points above.

Software and code

Policy information about [availability of computer code](#)

Data collection

Vevo LAZR Imaging System, CHI660E, Nikon NIS Elements

Data analysis

Matlab R2017a, Origin 8.5, ABAQUS, Image J

For manuscripts utilizing custom algorithms or software that are central to the research but not yet described in published literature, software must be made available to editors/reviewers. We strongly encourage code deposition in a community repository (e.g. GitHub). See the Nature Research [guidelines for submitting code & software](#) for further information.

Data

Policy information about [availability of data](#)

All manuscripts must include a [data availability statement](#). This statement should provide the following information, where applicable:

- Accession codes, unique identifiers, or web links for publicly available datasets
- A list of figures that have associated raw data
- A description of any restrictions on data availability

The authors declare that the main data supporting the results in this study are available within the paper and its Supplementary Information. The raw and analysed datasets generated during the study are available for research purposes from the corresponding authors on reasonable request.

Field-specific reporting

Please select the one below that is the best fit for your research. If you are not sure, read the appropriate sections before making your selection.

- Life sciences Behavioural & social sciences Ecological, evolutionary & environmental sciences

Life sciences study design

All studies must disclose on these points even when the disclosure is negative.

Sample size	Because of the absence of previous related research, we chose the sample size of n=13 for cats and n=7 for nude mice because the size was big enough for us to observe reliable and reproducible reactions on the bioanalytes.
Data exclusions	No data were excluded from this study.
Replication	All experiments were reliably reproduced using more than 3 technical repeats, and the success rate of implantation was over 95%. All conclusions were reproducible from these experiments.
Randomization	For the animal experiments, cats and nude mice were randomly allocated to the experimental group and the control group. For the artificial blood, the parameters were allocated on the basis of calibration by commercial instruments (peristaltic pump; Longer Precision Pump Co., Ltd, rotational rheometer; Thermofisher) so that the artificial blood had the same properties of the blood we were aiming to simulate. For photoacoustic analyses, cardiac muscle and brain tissue were chosen because they respectively represented hard and soft tissues under physiological status.
Blinding	Blinding was not performed, because there was no subjective test in this study.

Reporting for specific materials, systems and methods

We require information from authors about some types of materials, experimental systems and methods used in many studies. Here, indicate whether each material, system or method listed is relevant to your study. If you are not sure if a list item applies to your research, read the appropriate section before selecting a response.

Materials & experimental systems

n/a	Included in the study
<input type="checkbox"/>	<input checked="" type="checkbox"/> Antibodies
<input checked="" type="checkbox"/>	<input type="checkbox"/> Eukaryotic cell lines
<input checked="" type="checkbox"/>	<input type="checkbox"/> Palaeontology
<input type="checkbox"/>	<input checked="" type="checkbox"/> Animals and other organisms
<input checked="" type="checkbox"/>	<input type="checkbox"/> Human research participants
<input checked="" type="checkbox"/>	<input type="checkbox"/> Clinical data

Methods

n/a	Included in the study
<input checked="" type="checkbox"/>	<input type="checkbox"/> ChIP-seq
<input checked="" type="checkbox"/>	<input type="checkbox"/> Flow cytometry
<input checked="" type="checkbox"/>	<input type="checkbox"/> MRI-based neuroimaging

Antibodies

Antibodies used	Anti-CD11b antibody (clone EPR1344, catalog number ab133357, Lot number GR215253-10, Abcam, 1:300 dilution); Goat anti-Rabbit IgG (H+L) Cross-Adsorbed Secondary Antibody, Cy3 (GB21303, Servicebio, 1:300 dilution)
Validation	Rabbit anti-CD11b (ab133357, Abcam) Validated in Hill, David A., et al. Distinct macrophage populations direct inflammatory versus physiological changes in adipose tissue. Proceedings of the National Academy of Sciences 115, 22 (2018): 201802611.

Animals and other organisms

Policy information about [studies involving animals](#); [ARRIVE guidelines](#) recommended for reporting animal research

Laboratory animals	This study used ten adult female cats (<i>Felis catus</i>) and three adult male cats aged from one year to two years with weights of 1.5–2.5 kg. For tumour analyses, seven weeks female BALB/c nude mice (about 20 g in weight) were used.
Wild animals	The study did not involve wild animals.
Field-collected samples	The study did not involve samples collected from the field.
Ethics oversight	The experiment protocols were approved by the Animal Experimentation Committee of Fudan University. All animals were treated in accordance with guidelines for the care and use of experimental animals described by the National Institutes of Health and Fudan University.

Note that full information on the approval of the study protocol must also be provided in the manuscript.